




Fast X-ray ptychography: towards nanoscale imaging of large volume of brain

Silvia Cipiccia^{1,a}, Michela Fratini^{2,3,b}, Ecem Erin^{1,c}, Marco Palombo^{4,d}, Silvia Vogel^{5,e} , Max Burian^{5,f}, Fenglei Zhou^{1,6,g}, Geoff J. M. Parker^{1,7,h}, Darren J. Batey^{8,i}

¹ Department of Medical Physics and Biomedical Engineering, University College London, Malet Place Engineering, Gower St, London WC1E 6BT, UK

² Institute of Nanotechnology, CNR-Nanotec, Piazzale Aldo Moro 5, 00185 Rome, Italy

³ Santa Lucia Foundation, via Ardeatina 356, 00179 Rome, Italy

⁴ Cardiff University Brain Research Imaging Centre, Cardiff University, Maindy Road, Cardiff CF24 4HQ, UK

⁵ DECTRIS Ltd., Taefernweg 1, 5405 Baden-Daettwil, Switzerland

⁶ BioPhantoms Ltd., Watson House, 4 Mill Park, Cambridge CB1 2FH, UK

⁷ Bioxydyn Limited, St James Tower, 7 Charlotte Street, Manchester M1 4DZ, UK

⁸ Diamond Light Source, Harwell Science and Innovation Campus, Fermi Avenue, Didcot OX11 0DE, UK

Received: 19 December 2023 / Accepted: 28 April 2024

© The Author(s) 2024

Abstract X-ray ptychography, a scanning coherent diffraction imaging technique, is one of the most used techniques at synchrotron facilities for high resolution imaging, with applications spanning from life science to nano-electronics. In the recent years there has been a great effort to make the technique faster to enable high throughput nanoscale imaging. Here we apply a fast ptychography scanning method to image in 3D $10^6 \mu\text{m}^3$ of brain-like phantom at 3 kHz, in a 7 h acquisition with a resolution of 270 nm. We then present the latest advances in fast ptychography by showing 2D images acquired at 110 kHz by combining the fast-acquisition scheme with a high-acquisition rate prototype detector from DECTRIS Ltd. We finally review the experimental outcome and discuss the prospective use of fast ptychography schemes for the investigation of mm^3 size samples of brain-like phantom, by extrapolating the current results to the high coherent flux scenario of diffraction limited storage rings.

1 Introduction

Ptychography is a scanning coherent imaging technique which allows to image samples at resolutions beyond the optical limits of the imaging system [1]. A standard ptychographic acquisition consists of moving the sample across a coherent beam at overlapping steps, while recording the diffraction patterns, typically in the far field. The diffraction patterns are subsequently inverted using an iterative algorithm [2–5] to form the image of the sample. When combined with the penetration power of X-rays, ptychography has enabled scientific breakthroughs in a range of fields, from magnetism [6] to nanoelectronics [7]. Ptychography has proven to be very suitable also to image weakly absorbing samples, such as biological soft tissues, as it is sensitive to small changes of electron density [8].

X-ray ptychography requires long acquisition times when compared to other nano-scale techniques (e.g. transmission X-ray microscope). This is due to large overheads when scanning sample precisely to thousands of positions for a single projection. These long acquisition times have prevented the deployment of X-ray ptychography for imaging large sample volumes or for dynamic/multidimensional studies such as X-ray near edge spectroscopy imaging. To overcome this limitation, in the latest years the ptychography community has strived to reduce the acquisition time by developing new scanning strategies [9], including multibeam ptychography [10] and fly-scanning methods [11–19]. The multibeam approach consists of using a coded aperture to

Silvia Cipiccia and Darren J. Batey have contributed equally to this work.

^a e-mail: s.cipiccia@ucl.ac.uk (corresponding author)

^b e-mail: michela.fratini@gmail.com

^c e-mail: ecem.erin.23@ucl.ac.uk

^d e-mail: palombom@cardiff.ac.uk

^e e-mail: silvia.vogel@dectris.com

^f e-mail: max.burian@dectris.com

^g e-mail: fenglei.zhou@ucl.ac.uk

^h e-mail: geoff.parker@ucl.ac.uk

ⁱ e-mail: darren.batey@diamond.ac.uk

generate multiple beamlets spatially separated at the sample and overlapping in the detector at the far field, to reduce the number of steps required for an acquisition. The fly-scanning approach consists of recording diffraction patterns while moving the sample along a continuous trajectory to reduce the motors' stop-start overhead at each position. Thanks to these advances, fast X-ray ptychography now has the potential to image large samples (100's of μm^2), of soft biological tissues, such as from lung, heart or brain.

The study of the human brain is indeed a phenomenal challenge due to the complexity of the tissue and its multiscale nature: from nanoscale molecular features to centimetres long structural connections. Understanding the interplay between its structure and function is key to diagnose, prevent and possibly treat diseases such as dementia. International projects are bringing together scientists around the world to tackle the problem [20, 21]. There is the need for a transformative tool to image the whole human brain *in vivo* at high (sub-micron) resolution. Diffusion magnetic resonance imaging (dMRI) is a promising MRI technique for this purpose. In dMRI the brain structure at cellular (microscopic) scale can be inferred via biophysical modelling of the diffusion of water molecules during *in vivo* measurements [22]. One of the main challenges is the validation of the model-based estimates of the microstructural features of the investigated tissue. The ideal benchmarking dataset is a large volume of brain sample of the order of 1mm^3 , that is approximately the size of a complete cortical microcircuit [23], imaged with nanoscale resolution.

So far this has been achieved with expansion microscopy [24] and multibeam scanning electron microscopy [25]. In the first, the sample gets infused with hydrogel and doing so expanded and made more transparent to be inspected with optical light [26]. In the second, tens of simultaneous electron beams illuminate the sample, which is prepared in thin slices, due to the low penetration power of electrons. Both approaches are destructive: hard X-ray fast ptychography could be a valuable non-destructive alternative to the above methods thanks to the higher penetration properties of hard X-rays with respect to electrons or soft X-rays, and the increased resolution with respect to visible light due to the shorter wavelength. Here we investigate its potential.

As a first step toward using ptychography for this purpose, we apply a high-speed ptychography setup at the I13-1 beamline of Diamond Light Source [19] to image $10^6\mu\text{m}^3$ volume of polymer phantom, which mimics the tissue structure within the brain, in 7 h. We also present the latest results where we performed fast ptychographic imaging of a 2D test resolution target at 110 kHz acquisition rate by combining fly-scanning and a prototype detector from DECTRIS Ltd. Based on the latest results we discuss the future perspectives in terms of scanning speed and resolution.

2 Results

2.1 Large volume imaging

We imaged a biomimetic phantom based on polymer microcylinders [27] made of polycaprolacton (PCL) [28] intended to mimic the axons found in the white matter of the brain. This type of phantom has comparable density to brain tissue, it has been extensively characterised [28] and proven to be representative of the brain white matter tissue, and it is used as validation tool for new approaches [29]. It is often considered as a superior alternative to software phantoms and histological samples. Indeed physical phantoms, similarly to virtual samples [30], are more controllable in structure than histological samples. Moreover, unlike the virtual samples, they offer the advantage of being scanned using identical procedures as for real samples. This allows realistic signal-to-noise ratios and image artefacts to be taken into account.

The sample was cut down with a scalpel in a quasi-cylindrical shape of $100\mu\text{m}$ diameter and imaged at the I13-1 beamline at Diamond Light Source [31] using a fly-scanning method based on the approach described in detail in ref [19]. In this method, the maximum acquisition rate is set by the maximum acquisition rate of the detector. For each detector acquisition a sample position is stored. In the eventuality the readout of the sample position is slower than the detector acquisition, extra positions get generated during the reconstruction by interpolating in-between the recorded positions. To improve the throughput of ptychographic tomography, the framework was upgraded with respect to ref [19] with a faster position capture device, the PandA trigger box, capable of up to 10 kHz acquisition rate [32], and the system was adapted such that all files were streamed continuously to disk.

The experimental setup is sketched in Fig. 1. The sample was illuminated with an 11 keV monochromatic X-ray beam of $3.5\mu\text{m}$ in diameter generated using a $400\mu\text{m}$ diameter blazed Fresnel zone plate [33] (FZP) with a 200nm outermost zone width. The sample was placed a few millimetres downstream of the FZP focal plane. For each 2D projection, the sample was scanned in a 1000×100 grid with a snake-like motion by continuously moving the horizontal motor back and forth (fast axis) and stepping in the vertical axis downwards (slow axis), see Fig. 1. The EIGER 500K photon counting detector (1030×514 pixels, $75\mu\text{m}$ pixel size) was placed at 5.1 m downstream of the sample. Diffraction frames were acquired during the horizontal motion every $0.15\mu\text{m}$, the vertical step was $0.5\mu\text{m}$, corresponding to a field of view $150 \times 50\mu\text{m}^2$. Frames were recorded at 2874 Hz with an exposure time of $340\mu\text{s}$, corresponding to $220\mu\text{m}^2/\text{s}$. All the sample positions were captured using a PandA trigger box without need for interpolation.

We acquired 501 projections over a angular range of 180° allowing us to image $10^6\mu\text{m}^3$ in 7 h, which corresponds to $39\mu\text{m}^3/\text{s}$

Each projection was reconstructed, from 128×128 pixels cropped data, with 50 iterations of the ePIE algorithm [2] as implemented in the PtyREX software [34] with a reconstructed pixel size of 60 nm, using 4 spatial modes.

The projections were then aligned using the approach by Gursoy [35] and reconstructed using the gridrec algorithm implemented in tomopy [36]. The results are shown in Fig. 2. The spatial resolution was estimated to be 270 nm on the xz slice Fig. 2b, using

Fig. 1 Experimental setup. The monochromated X-ray beam is focused down to the sample using Fresnel zone plate optics. The sample is scanned in a snake like motion in a continuous fashion the horizontal axis (fast axis, black arrow) and stepped vertically (slow axis, red line). A detector in the far field records the diffraction patterns

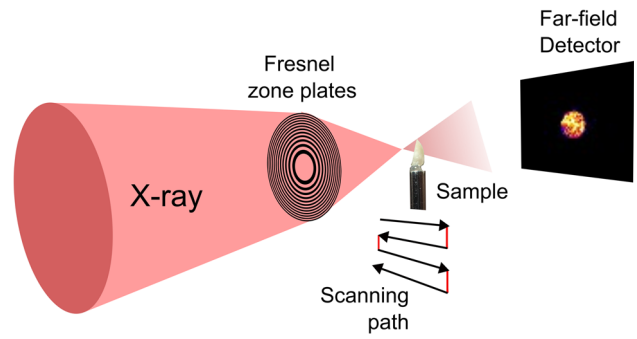
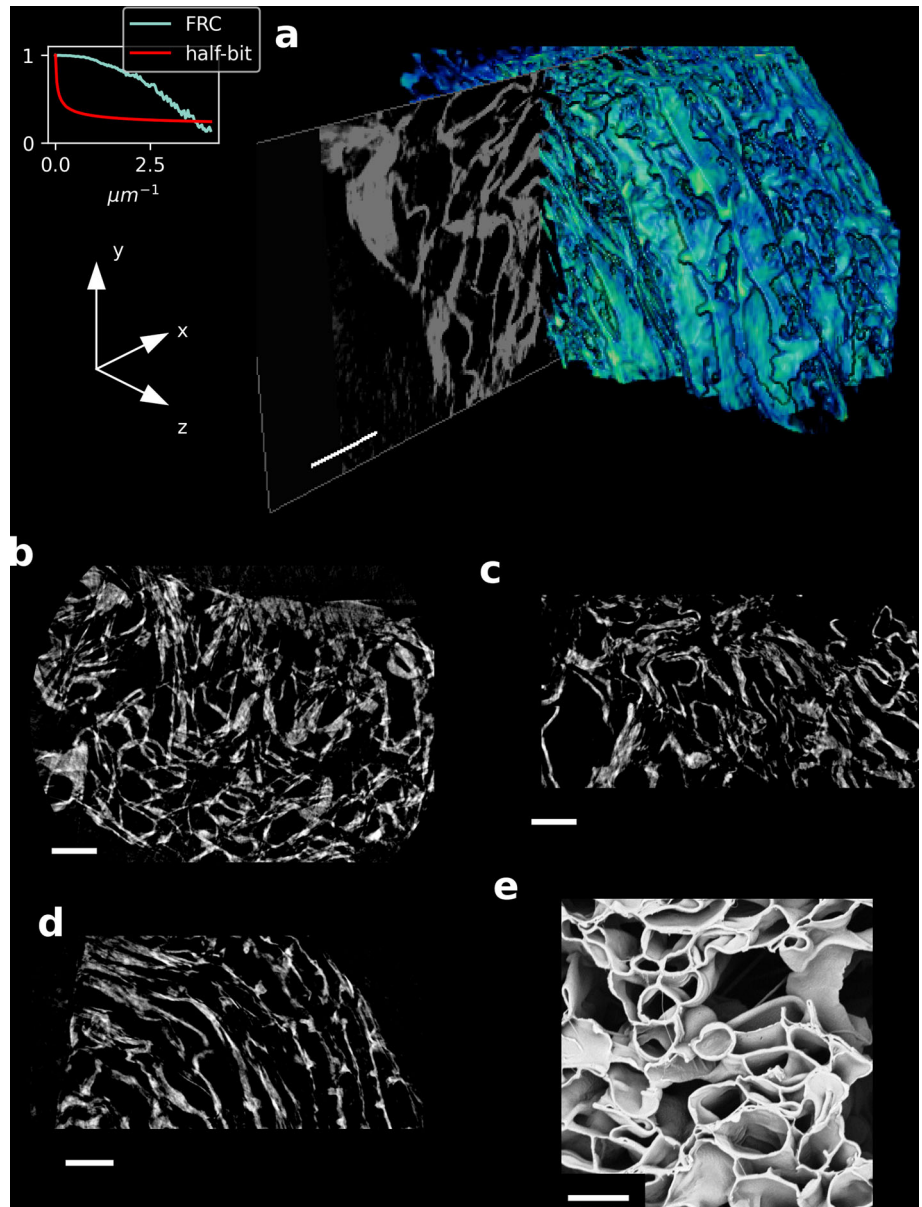
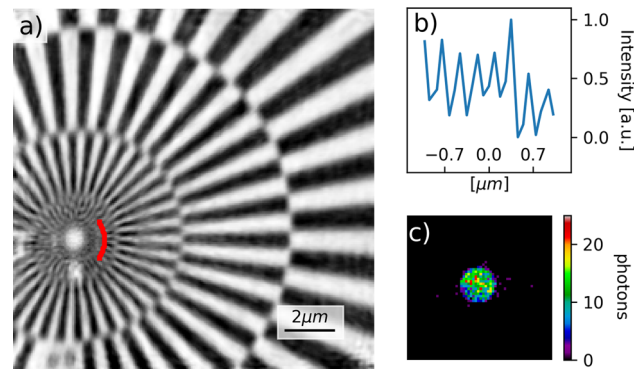


Fig. 2 3D image of a brain-like phantom mimicking a bundle of axons in the white matter [28]. **a** rendered 3D volume. Inset: Fourier ring correlation on orthoslice **b**, representative also for orthoslice **c** and **d**. **b–d** Orthoslices through the volume in the xz, xy and zy plane, respectively. **e** SEM image of a similar sample of the phantom materials showing its cross-sectional morphology. The white scale bars in all the plots correspond to 10 μ m



an implementation of the Fourier ring correlation [37] provided as part of the BIOP ImageJ plugin [38] (see Fig. 2a inset). Two independent images were generated by splitting the original in even and odd indexes.

Fig. 3 110 kHz ptychography: **a** Phase image of a Siemens star test patten scanned at 110 kHz. **b** Line profile extracted from the **a** (red line) showing a resolution of 285 nm. **c** A typical diffractogram captured during the 110 kHz scan. The maximum photons count is 22 photons per pixel



2.2 110 kHz ptychography

The ultimate speed of the fast ptychography scanning method applied in this study [19] is determined by the detector acquisition rate. In the experiment presented in Sect. 2.1, this is 3 kHz, the maximum acquisition rate for the EIGER 500 K in continuous read/write mode. Recently a new photon counting prototype detector has been developed by DECTRIS Ltd capable of 120 kHz acquisition rate.

2.2.1 120 kHz photon counting detector

The hybrid photon counting detector is a prototype of the SELUN detector being developed by DECTRIS Ltd. The detector has a pixel array of 192×192 pixels at $100 \times 100 \mu\text{m}^2$ pixel size, comprising an active area of $19.2 \times 19.2 \text{ mm}^2$. Each pixel consists of two 12 Bit counters for continuous readout at 20 kHz. Effectively, the ASIC can be operated in an 8-Bit Floating Point compression scheme which enables framerates of up to 30 kHz. Additionally, by on chip binning of 2×2 pixels, the framerate can be further increased to 120 kHz with an effective pixel size of $200 \times 200 \mu\text{m}^2$. Based on preliminary measurements and simulations of the performance of the ASIC of the SELUN, the detector development aims to reach a count rate of 50 Mphotons/pixel/s unbinned, and 4 times higher, that is 200 Mphotons/pixel/s, with a 2×2 binning [39, 40].

2.2.2 2D imaging at 110 kHz

We have performed a ptychography acquisition at 110 kHz to image a Siemens star test pattern using the prototype detector presented in Sect. 2.2.1 in a 2×2 binning mode. The experiment was performed with similar experimental conditions as described in 2.1. The detector was placed 5.1 m downstream the sample and the X-ray energy was set to 11.1 keV. The sample positions were recorded with the PandA trigger box at 10 kHz. The missing intermediate positions were generated during the reconstruction by interpolation. A typical diffractogram obtained with an exposure of $7 \mu\text{s}$ is shown in Fig. 3c. The maximum number of counts recorded is 22 photons per pixel due to the very short exposure time, which corresponds to 2×10^6 photons/pixel/s and a total coherent flux at the sample of 2×10^8 photons/s. To preserve the total photon statistics per resolution element, we imaged a $20 \times 20 \mu\text{m}^2$ area of the sample by acquiring over a 2800×20 grid, that is a horizontal step size of 7 nm , which corresponds to $800 \mu\text{m}^2 \text{ s}^{-1}$. Because there were no photons counted beyond 32 pixels from the centre of the diffracted beam, the SELUN data were cropped to 64×64 pixels. The image was reconstructed from the cropped data with 50 iterations of the PtyREX ePIE module, by upsampling of a factor 2 [41] to compensate for the larger pixel size ($200 \times 200 \mu\text{m}^2$), by including two spatial modes and the annealing approach to correct for position errors due to the interpolation process [42]. The reconstructed phase image is shown in Fig. 3. The reconstructed image pixel size is 88 nm (set by the cropping) and the measure resolution is 285 nm as shown with the line profile in Fig. 3b.

3 Discussion and conclusion

In Sect. 2.1 we have shown 3D imaging of a brain-like sample obtained with a $39 \mu\text{m}^3 \text{ s}^{-1}$ X-ray ptychographic tomography. In the experiment the scanning rate was limited to 3 kHz by the maximum continuous acquisition rate of the EIGER 500 k photon counting detector.

In Sect. 2.2 we have demonstrated the feasibility of ptychographic imaging at 110 kHz by coupling the fast ptychography method of ref [19] with a new DECTRIS Ltd prototype detector. The summary of the two experimental parameters is reported in Table 1. During the 110 kHz scan, to compensate for the low photon statistics of each frame, we reduced the step size in the fast axis (horizontal movement) with respect to the experiment in Sect. 2.1. In terms of $\mu\text{m}^2 \text{ s}^{-1}$, this means we scanned the sample 4 times

Table 1 Experimental parameters

	3 kHz	110 kHz
Detector	EIGER	SELUN
Pixel size	75 μm	¹ 200 μm
Active area (pixels)	1030 \times 514	296 \times 96
Active area (mm)	77 \times 38	19 \times 19
Sample-to-detector distance	5.1 m	5.1 m
Exposure time	340 μs	7 μs
Imaged area	150 \times 50 μm^2	20 \times 20 μm^2
³ Cropped area	128 \times 128	64 \times 64
Reconstructed pixel size	60 nm	88 nm

¹Valid for acquisition rates above 30 kHz. 100 μm below 30 kHz

²Valid for acquisition rates above 30 kHz. 192 \times 192 below 30 kHz

³Area in pixels beyond which no photons are detected. Cropping applied for the ptychographic reconstruction

faster than with the EIGER 500k detector. However, the scheme would allow a 36 times faster acquisition. To exploit this potential in full, a higher coherent flux is needed.

With the advent of 4th generation light sources (diffraction limited storage rings), the coherent flux increases up to a factor 100 with respect to 3rd generation light sources. This is already available at synchrotron facilities around the world (e.g. ESRF, MAX-IV, etc) and soon coming at others (Advanced Photon Source, Paul Scherrer Institute and Diamond Light Source). This extra two orders of magnitude flux increase would correspond, in a geometry similar to that described in this manuscript, up to 200×10^6 photons/pixel/s in the central disk, which is within the expected performance of the SELUN detector.

Regarding achievable resolution and future scaling, it is worthwhile noting that the active area of the current design of the SELUN detector is at the best half of the EIGER 500k active area (see Table 1). In ptychography the maximum resolution achievable depends on the angular coverage of the detector area. That is:

$$dx = \frac{\lambda z}{D} \quad (1)$$

where dx is the reconstructed pixel size/maximum resolution, λ is the beam wavelength, z is the sample-detector distance and D is the width of the detector active area. To achieve with the SELUN the same nominal resolution as with the EIGER 500k, the detector would need to be closer to the sample (half of the distance). In the experiment reported, the sample-detector distance was the same for the EIGER and the SELUN, so the maximum resolution achievable was different for the two setups and, respectively, equal to 15 nm for the EIGER and 30 nm for the SELUN. However, we decided not to move the SELUN detector closer to the sample to achieve the same nominal resolution, because the resolution was dominated by the low photon statistics: already at 5.1 m at 110 kHz acquisition there were no photon counts beyond 32 pixels from the centre of the beam. Indeed, the reconstructed dataset of Fig. 3 is obtained from a 64 \times 64 pixel cropped area of the SELUN detector, corresponding to a reconstructed pixel size of 88 nm.

Taking the above into account, we can extrapolate the results for the brain phantom obtained with the EIGER at 3 kHz (Fig. 2), toward 110 kHz scanning of brain tissue. Since the brain phantoms have similar electron density and structural properties as brain tissue [28], that is comparable scattering properties, we can expect to achieve a similar resolution of 270 nm in 3D on brain tissue at 110 kHz with a factor 50 increase in flux. The factor 50 corresponds to the ratio between the exposure time for the 3 kHz and the 110 kHz, respectively (see Table 1). Combining the factor 100 increase in coherent flux due to storage rings upgrade to higher efficiency pre-focussing optics such as KB mirrors instead of Fresnel zone plates, an additional increase in flux at the sample of more than a factor 5 can be foreseen. Therefore, in total we expect a flux over an order of magnitude higher than required for matching Fig. 2. A study by Deng et al. [43] shows that an increase of one order of magnitude in average flux on the sample corresponds to an increase of a factor 2 in resolution. Based on this scaling, it is therefore reasonable to expect 100 nm resolution to be achievable for brain-like samples at 110 kHz ptychographic acquisition in the near future. To be noted that to remain within 200 Mphotons/pixel/s in the central disk, the higher future flux would need to be distributed across the whole detector active area, for example by using a larger numerical aperture pre-focussing optics or a diffuser.

As described in Sect. 2.2.2, during the 110 kHz acquisition we compensated for the low photon statistics by reducing the scanning step size. This will not be any longer required with the estimated increase of coherent flux at diffraction limited storage rings and, in this scenario with the 110 kHz fast ptychography setup, we expect to be possible to scan samples up to $6000 \mu\text{m}^2 \text{s}^{-1}$. Acquiring a single 1 mm^2 projection will take 170 s and to image a 3D 1 mm^3 at 100 nm resolution, the acquisition would last 19 days (based on 10^4 projections collected over 180°, see Appendix A for further details).

Further reduction of the acquisition time can be achieved by combining the fly-scanning to the multibeam approach. For example, using 9 probes as in ref [10], the acquisition time for 1 mm^3 of brain would become as short as 2 days. Moreover, the overlap constraint can be relaxed with the combined ptycho-tomography reconstruction approach by Gursoy [44]. This is expected to provide at least a further factor 3 in the reduction of the scan duration. Combining all these developments together, the acquisition time for 1 mm^3 of brain would become as short as 1 day.

To image a large volume of brain at the nanoscale, there are other outstanding challenges that need to be solved. These include but are not limited to:

- **Radiation damage:** ptychography is considered a dose effective technique since it does not require imaging lenses [45]. The expected total dose delivered to a brain-like phantom sample during a ptychography acquisition to achieve 100 nm resolution, is of the order of the MGy (see Appendix B for the calculations). A dedicated study is required to understand the radiation damage and the effects of the dose fractionation implied by the scanning. Beside this, different strategies can be explored to prevent the deterioration of the sample during the acquisition, such as performing the experiment in a cryo-environment [46] and/or using higher photon energy to reduce the absorption.
- **Sample preparation:** while the best preparation strategy specifically for ptychography needs to be identified, this can be based upon existing studies present in literature on sample preparation for microtomography [47–50].
- **Standard ptychographic reconstruction algorithms** are based on the assumption that multiple scattering does not occur. This condition is violated when thick samples are imaged and a multislice approach [51] is required to take the multiple scattering into account. This method has been proven successful in modelling a few slices (less than ten) of samples of various thickness, from 100 μm [52] to 1 mm [53]. This still needs to be proven to deal effectively with tens of slices.
- **Data processing:** 1 day acquisition at 110 kHz would produce about 40TB of data. There is need for faster converging, highly parallelisable ptychographic reconstruction algorithms. The community is exploring several routes including deep learning approaches [54, 55].

The study presented here it is not the end of the story but a significant step toward imaging 1 mm^3 at the nanoscale, which would represent a terrific tool to unravel the complexity of the human brain.

Supplementary Information The online version contains supplementary material available at <https://doi.org/10.1140/epjp/s13360-024-05224-w>.

Author contributions MF and FZ prepared the composite polymeric phantoms. SC, DB, MF, MB, SV and MP performed the experiment. SC, EE and DB performed the data analysis. SC, DB, MF, GP and MP contributed to the data interpretation. SC wrote the manuscript. All the Authors contributed to the review of the manuscript.

Funding This work is supported by EPSRC New Investigator Award EP/X020657/1. MP is supported by UKRI Future Leaders Fellowship (MR/T020296/2). We thank the Diamond Light Source for the beamtime MG34189-1 and MG32306-2.

Data availability The manuscript has associated data in a data repository. The authors confirm that all of the data used in this study are available upon reasonable request by contacting s.cipiccia@ucl.ac.uk.

Code availability Not applicable.

Declarations

Conflict of interest The authors declare no Conflict of interest.

Ethical approval Not applicable.

Consent to participate Not applicable.

Consent for publication all the Authors give consent for the publication.

Open Access This article is licensed under a Creative Commons Attribution 4.0 International License, which permits use, sharing, adaptation, distribution and reproduction in any medium or format, as long as you give appropriate credit to the original author(s) and the source, provide a link to the Creative Commons licence, and indicate if changes were made. The images or other third party material in this article are included in the article's Creative Commons licence, unless indicated otherwise in a credit line to the material. If material is not included in the article's Creative Commons licence and your intended use is not permitted by statutory regulation or exceeds the permitted use, you will need to obtain permission directly from the copyright holder. To view a copy of this licence, visit <http://creativecommons.org/licenses/by/4.0/>.

Appendix A: Number of projections for 3D imaging of 1 mm^3 at 100 nm resolution

For a 1 mm^3 sample, we can assume each projection to have an area of $1 \times 1\text{ mm}^2$. Aiming for a resolution of 100 nm, the maximum pixel size of each projection has to be at the maximum 100 nm. Therefore, each projection will have $10^4 \times 10^4$ pixels. In tomography, the rule of thumb for the number of projection required is to match the number of pixels in the projections width, to be more precise, $N_{proj} > \frac{\pi}{2} n_{pixels}$, where N_{proj} is the number of projections, and n_{pixels} is the width of the projection in pixels. This comes from the need of sampling correctly in the Fourier space, based on the central slice theorem. This is a the fundamental concept of the tomography theory and reconstruction, and is extensively covered in the literature, for example in [56].

Table 2 Dose estimation for 1 mm³ scan of brain sample

Photon energy	¹ Photon flux at sample	Scan duration	² Absorption	Sample volume	Sample mass
11 keV	10 ¹¹ photons/s	24 hours	0.35	1 mm ³	10 ⁻⁶ kg

¹ Diffraction limited storage ring scenario

² 11 keV through 1 mm thick soft tissue. Based on the NIST data for X-ray interaction cross sections and material densities

Appendix B: Dose estimation scaling for 3D ptychography at 100 kHz at diffraction limited storage rings

The experiments reported in this manuscript have been carried out at I13-1 beamline where the coherent photon flux on the sample at 11 keV is 2×10^8 photons/s. In the scenario of high efficiency pre-focussing optics combined with a diffraction limited storage ring, the expected photon flux on the sample is 10^{11} photons/s. This corresponds to a total of 0.48 J/day deposited on the sample. For a tissue sample of 1 mm³ this is equivalent to a dose of 5 MGy for the 3D scan. Table 2 summarises the parameters used for this estimation.

References

- J.M. Rodenburg, H.M.L. Faulkner, A phase retrieval algorithm for shifting illumination. *Appl. Phys. Lett.* **85**, 4795–4797 (2004). <https://doi.org/10.1063/1.1823034>
- A. Maiden, J. Rodenburg, An improved ptychographical phase retrieval algorithm for diffractive imaging. *Ultramicroscopy* **109**, 1256–62 (2009). <https://doi.org/10.1016/j.ultramic.2009.05.012>
- M. Guizar-Sicairos, J.R. Fienup, Phase retrieval with transverse translation diversity: a nonlinear optimization approach. *Opt. Express* **16**, 7264–7278 (2008). <https://doi.org/10.1364/oe.16.007264>
- B. Enders, P. Thibault, A computational framework for ptychographic reconstructions. *Proc. R. Soc. A Math. Phys. Eng. Sci.* **472**(20162196), 0640 (2018). <https://doi.org/10.1098/rspa.2016.0640>
- S. Marchesini et al., SHARP: a distributed GPU-based ptychographic solver. *J. Appl. Crystallogr.* **49**, 1245–1252 (2016). <https://doi.org/10.1107/S1600576716008074>
- C. Donnelly et al., Three-dimensional magnetization structures revealed with X-ray vector nanotomography. *Nature* **547**, 328–331 (2017). <https://doi.org/10.1038/nature23006>
- M. Holler et al., Three-dimensional imaging of integrated circuits with macro- to nanoscale zoom. *Nat. Electron.* **2**, 464–470 (2019). <https://doi.org/10.1038/s41928-019-0309-z/>
- A. Bhartiya et al., X-ray ptychography imaging of human chromosomes after low-dose irradiation. *Chromosome Res.* **29**, 419–420 (2021). <https://doi.org/10.1007/s10577-021-09668-z>
- M. Odstrcil, M. Lebugle, T. Lachat, J. Raabe, M. Holler, Fast positioning for X-ray scanning microscopy by a combined motion of sample and beam-defining optics. *J. Synchrotron Radiat.* **26**, 504–509 (2019). <https://doi.org/10.1107/S160057751801785X>
- M. Lyubomirskiy et al., Multi-beam X-ray ptychography using coded probes for rapid non-destructive high resolution imaging of extended samples. *Sci. Rep.* **12**, 6203 (2022). <https://doi.org/10.1038/s41598-022-09466-5>
- Y. Jiang et al., Achieving high spatial resolution in a large field-of-view using lensless X-ray imaging. *Appl. Phys. Lett.* **119**, 124101 (2021). <https://doi.org/10.1063/5.0067197>
- M.W.M. Jones et al., High-speed free-run ptychography at the Australian Synchrotron. *J. Synchrotron Radiat.* **29**, 480–487 (2022). <https://doi.org/10.1107/S1600577521012856>
- M. Odstrčil, M. Holler, M. Guizar-Sicairos, Arbitrary-path fly-scan ptychography. *Opt. Express* **26**, 12585–12593 (2018). <https://doi.org/10.1364/OE.26.012585>
- X. Huang et al., Fly-scan ptychography. *Sci. Rep.* **5**, 9074 (2015). <https://doi.org/10.1038/srep09074>
- J.N. Clark, X. Huang, R.J. Harder, I.K. Robinson, Continuous scanning mode for ptychography. *Opt. Lett.* **39**, 6066–6069 (2014). <https://doi.org/10.1364/OL.39.006066>
- J. Deng et al., Continuous motion scan ptychography: characterization for increased speed in coherent X-ray imaging. *Opt. Express* **23**, 5439–51 (2015). <https://doi.org/10.1364/OE.23.005438>
- J. Deng et al., The Velociprobe: An ultrafast hard X-ray nanoprobe for high-resolution ptychographic imaging. *Rev. Sci. Instrum.* **90**, 083701 (2019). <https://doi.org/10.1063/1.5103173>
- P.M. Pelz et al., On-the-fly scans for X-ray ptychography. *Appl. Phys. Lett.* **105**, 251101 (2014). <https://doi.org/10.1063/1.4904943>
- D. Batey, C. Rau, S. Cipiccia, High-speed X-ray ptychographic tomography. *Sci. Rep.* **12**, 7846 (2022). <https://doi.org/10.1038/s41598-022-11292-8>
- Human brain project. <https://www.humanbrainproject.eu/en/>
- Human connectome project. <https://www.humanconnectome.org/>
- D.C. Alexander, T.B. Dyrby, M. Nilsson, H. Zhang, Imaging brain microstructure with diffusion mri: practicality and applications. *NMR Biomed.* **32**, e3841 (2019). <https://doi.org/10.1002/nbm.3841>
- W. Yin et al., A petascale automated imaging pipeline for mapping neuronal circuits with high-throughput transmission electron microscopy. *Nat. Commun.* (2020). <https://doi.org/10.1038/s41467-020-18659-3>
- W. Yang, R. Yuste, Brain maps at the nanoscale. *Nat. Biotechnol.* **37**, 378–380 (2019). <https://doi.org/10.1038/s41587-019-0078-2>
- R.L. Schalek et al., Volume Electron Microscopy Workflows for the study of Large-Scale Neural Connectomics. *Microsc. Microanal.* **29**, 1209–1211 (2023). <https://doi.org/10.1093/micmic/ozad067.622>
- R. Gao et al., Cortical column and whole-brain imaging with molecular contrast and nanoscale resolution. *Science* **363**, eaau8302 (2019). <https://doi.org/10.1126/science.aau8302>
- D.J. McHugh et al., A biomimetic tumor tissue phantom for validating diffusion-weighted mri measurements. *Magn. Reson. Med.* **80**, 147–158 (2018). <https://doi.org/10.1002/mrm.27016>

28. F.-L. Zhou, P.L. Hubbard, S.J. Eichhorn, G.J.M. Parker, Coaxially electrospun axon-mimicking fibers for diffusion magnetic resonance imaging. *ACS Appl. Mater. Interfaces* **4**, 6311–6316 (2012). <https://doi.org/10.1021/am301919s>
29. E.J. Canales-Rodríguez et al., Pore size estimation in axon-mimicking microfibers with diffusion-relaxation MRI. *Magn. Reson. Med.* (2024). <https://doi.org/10.1002/mrm.29991>
30. M. Palombo, D.C. Alexander, H. Zhang, A generative model of realistic brain cells with application to numerical simulation of the diffusion-weighted mr signal. *NeuroImage* **188**, 391–402 (2019). <https://doi.org/10.1016/j.neuroimage.2018.12.025>
31. C. Rau et al., Müller, B. & Wang, G. in *Operando and high-throughput multiscale-tomography*, eds. Müller, B. & Wang, G. Developments in X-ray Tomography XIII, Vol. 11840, 118401E. International Society for Optics and Photonics (SPIE, 2021). <https://doi.org/10.1117/12.2598470>
32. S. Zhang et al., PandABox: A Multipurpose Platform for Multi-technique Scanning and Feedback Applications (2018). <https://doi.org/10.18429/JACoW-ICALEPCS2017-TUAPL05>
33. S. Gorelick et al., High-efficiency Fresnel zone plates for hard X-rays by 100keV e-beam lithography and electroplating. *J. Synchrotron Radiat.* **18**, 442–446 (2011). <https://doi.org/10.1107/S0909049511002366>
34. D.J. Batey, Ptychographic imaging of mixed states (2014). <https://theses.whiterose.ac.uk/8524/>
35. D. Gürsoy et al., Rapid alignment of nanotomography data using joint iterative reconstruction and reprojection. *Sci. Rep.* **7**, 11818 (2017). <https://doi.org/10.1038/s41598-017-12141-9>
36. D. Gürsoy, F. De Carlo, X. Xiao, C. Jacobsen, Tomopy: a framework for the analysis of synchrotron tomographic data. *J. Synchrotron Radiat.* **21**, 1188–93 (2014). <https://doi.org/10.1107/S1600577514013939>
37. R.P.J. Nieuwenhuizen et al., Measuring image resolution in optical nanoscopy. *Nat. Methods* **10**, 557–562 (2013). <https://doi.org/10.1038/nmeth.2448>
38. A. Herbert, O. Burri, Fourier ring correlation imagej plugin (2016). https://github.com/BIOP/304_ijk-frc
39. P. Zambon, *Personal Communication* (Unpublished, DECTRIS Ltd, 2024)
40. P. Zambon et al., Kite: high frame rate, high count rate pixelated electron counting ASIC for 4d STEM applications featuring high-Z sensor. *Nucl. Instrum. Methods Phys. Res. Sect. A Accel. Spectrom. Detect. Assoc. Equip.* **1048**, 167888 (2023)
41. D.J. Batey et al., Reciprocal-space up-sampling from real-space oversampling in X-ray ptychography. *Phys. Rev. A* **89**, 043812 (2014). <https://doi.org/10.1103/PhysRevA.89.043812>
42. A. Maiden, M. Humphry, M. Sarahan, B. Kraus, J. Rodenburg, An annealing algorithm to correct positioning errors in ptychography. *Ultramicroscopy* **120**, 64–72 (2012). <https://doi.org/10.1016/j.ultramic.2012.06.001>
43. J. Deng et al., High-resolution ptychographic imaging enabled by high-speed multi-pass scanning. *Opt. Express* **30**, 26027–26042 (2022). <https://doi.org/10.1364/OE.460232>
44. D. Gürsoy, Direct coupling of tomography and ptychography. *Opt. Lett.* **42**, 3169–3172 (2017)
45. M. Holler et al., X-ray ptychographic computed tomography at 16 nm isotropic 3d resolution. *Sci. Rep.* (2014). <https://doi.org/10.1038/srep03857>
46. H. Tran et al., Alterations in sub-axonal architecture between normal aging and parkinson's diseased human brains using label-free cryogenic X-ray nanotomography. *Front. Neurosci.* (2020). <https://doi.org/10.3389/fnins.2020.570019>
47. E. Stefanutti et al., Assessment of the effects of different sample perfusion procedures on phase-contrast tomographic images of mouse spinal cord. *J. Instrum.* **13**, C03027 (2018). <https://doi.org/10.1088/1748-0221/13/03/C03027>
48. M. Töpperwien, F. van der Meer, C. Stadelmann, T. Salditt, Three-dimensional virtual histology of human cerebellum by X-ray phase-contrast tomography. *Proc. Natl. Acad. Sci. U. S. A.* (2018). <https://doi.org/10.1073/pnas.1801678115>
49. P. Parlanti et al., Size and specimen-dependent strategy for X-ray micro-CT and TEM correlative analysis of nervous system samples. *Sci. Rep.* (2017). <https://doi.org/10.1038/s41598-017-02998-1>
50. Y. Zhang et al., Sample preparation and warping accuracy for correlative multimodal imaging in the mouse olfactory bulb using 2-photon, synchrotron X-ray and volume electron microscopy. *Front. Cell Dev. Biol.* **10**, 880696 (2022). <https://doi.org/10.3389/fcell.2022.880696>
51. P. Li, A. Maiden, Multi-slice ptychographic tomography. *Sci. Rep.* (2018). <https://doi.org/10.1038/s41598-018-20530-x>
52. E.H.R. Tsai, I. Usov, A. Diaz, A. Menzel, M. Guizar-Sicairos, X-ray ptychography with extended depth of field. *Opt. Express* **24**, 29089–29108 (2016). <https://doi.org/10.1364/OE.24.029089>
53. Z. Hu, Y. Zhang, P. Li, D. Batey, A. Maiden, Near-field multi-slice ptychography: quantitative phase imaging of optically thick samples with visible light and X-rays. *Opt. Express* **31**, 15791–15809 (2023). <https://doi.org/10.1364/OE.487002>
54. X. Pan et al., An efficient ptychography reconstruction strategy through fine-tuning of large pre-trained deep learning model. *iScience* **26**, 108420 (2023). <https://doi.org/10.1016/j.isci.2023.108420>
55. A.V. Babu et al., Deep learning at the edge enables real-time streaming ptychographic imaging. *Nat. Commun.* **14**, 7059 (2023). <https://doi.org/10.1038/s41467-023-41496-z>
56. A. Maier, S. Steidl, V. Christlein, J. Hornegger, in *Lecture Notes in Computer Science*, Vol. 11111 (Switzerland: Springer International Publishing AG, 2018). https://doi.org/10.1007/978-3-319-96520-8_8